



# CHALMERS

## **Effect of large shear deformation on fatigue crack behavior in pearlitic rail steel**

DANIEL GREN



THESIS FOR THE DEGREE OF LICENTIATE OF ENGINEERING

Effect of large shear deformation on fatigue crack behavior in  
pearlitic rail steel

DANIEL GREN

Department of Industrial and Materials Science  
Division of Engineering Materials  
CHALMERS UNIVERSITY OF TECHNOLOGY  
Gothenburg, Sweden 2022

Effect of large shear deformation on fatigue crack behavior in pearlitic rail steel  
DANIEL GREN

© DANIEL GREN, 2022

Thesis for the degree of Licentiate of Engineering IMS-2022-08  
Department of Industrial and Materials Science  
Division of Engineering Materials  
Chalmers University of Technology  
SE-412 96 Gothenburg  
Sweden  
Telephone: +46 (0)31-772 1000

Chalmers Reproservice  
Gothenburg, Sweden 2022



Effect of large shear deformation on fatigue crack behavior in pearlitic rail steel  
Thesis for the degree of Licentiate of Engineering  
DANIEL GREN  
Department of Industrial and Materials Science  
Division of Engineering Materials  
Chalmers University of Technology

## ABSTRACT

The impacts from global warming and climate change continue to rise and securing the needs of future generations requires a transition to a climate-neutral society. Rail transportation, as being one of the safest and most energy efficient modes of transportation offers a sustainable alternative to fossil-fueled based transportation. There are however many challenges that must be addressed for rail transportation to be a viable option. Safety, functionality, reliability and economic feasibility must be ensured. The major challenge related to materials is rolling contact fatigue which impairs the safety and economic reliability. The key factor to mitigate the effect of rolling contact fatigue is to understand how the material behavior changes when the material is subjected to repeated rolling contact loading. The imposed loadings from the wheel/rail contact induces severe deformations in the near-surface region of the rail and leads to the formation of an aligned and anisotropic microstructure. Rolling contact fatigue cracks is often initiated in this region and crack propagation is promoted by the direction of the microstructure alignment. The shape of typical head checks for example, correlates well with the anisotropy in fracture toughness.

The aim of this thesis work is to better understand how the anisotropy developing in service changes the fracture and fatigue characteristics of rail steels. Fatigue crack growth experiments under uniaxial and pulsating torsional loading, on both undeformed and predeformed pearlitic rail steel R260 have been conducted. The material state of the predeformed material is similar to the material state in the near surface of deformed rails and was obtained by large shear deformation under compression. The fatigue crack propagation experiments showed that the fatigue life is dependent on the material state where predeformed material have longer fatigue life. The effect of predeformation on the crack growth direction was limited in uniaxial loading whilst dependent on the material state in torsional loading.

Keywords: Pearlitic steel, Fatigue crack propagation, Torsional loading, Uniaxial loading, Pre-deformation, Anisotropy



## PREFACE

This licentiate thesis was carried out at the Department of Industrial and Materials Science at Chalmers University of Technology from June 2019 to July 2022 within the research project MU35 "Characterization of crack initiation and propagation in anisotropic material". This research project has been a part of the research activities within the National Centre of Excellence CHARMEC (Chalmers Railway Mechanics). Parts of the funding was provided by the European Union's Horizon 2020 research and innovation programme in the projects In2Track2 and In2Track3 under grant agreements Nos 826255 and 101012456. The project was carried out under supervision of Professor Johan Ahlström.

## ACKNOWLEDGEMENTS

First and foremost, I would like to thank my supervisor Johan Ahlström for the generous support, encouragement and guidance throughout the project. You are a good friend and a better supervisor cannot be found. I am very thankful for being given the opportunity of this research project. I would also like to thank Dr Knut Andreas Meyer for all the help in the workshop and for the co-authorship in **Paper B**. A special thank you to my colleagues and friends for creating an enjoyable and supportive working environment.

To my friends from Arvika and Brålanda, thank you for being around and I enjoy spending time with you. Last but not least, I would like to thank my girlfriend Erica, thank you for all your love and support.



# THESIS

This thesis consists of an extended summary and the following appended papers:

- Paper A** Daniel Gren, Johan Ahlström, Fatigue crack propagation on uniaxial loading of biaxially pre-deformed pearlitic rail steel. *Manuscript* (2022)
- Paper B** Daniel Gren, Knut Andreas Meyer, Effects of predeformation on torsional fatigue in R260 rail steel. *Manuscript* (2022)

The appended papers were prepared in collaboration with the co-authors. The author of this thesis has contributed as follows: **Paper A** responsible for the major progress of the work i.e., planning of paper, experimental work, interpretation of results and writing. **Paper B** the planning of the work, interpretation of the results and writing were done together with Dr Knut Andreas Meyer and the author of this thesis was responsible for the major progress of the experimental work and writing the original draft.



# CONTENTS

<b>Abstract</b>	<b>i</b>
<b>Preface</b>	<b>iii</b>
<b>Acknowledgements</b>	<b>iii</b>
<b>Thesis</b>	<b>v</b>
<b>Contents</b>	<b>vii</b>
<b>I Extended Summary</b>	<b>1</b>
<b>1 Introduction</b>	<b>1</b>
1.1 Background . . . . .	1
1.2 Aim and scope . . . . .	2
<b>2 Theory</b>	<b>3</b>
2.1 Railway-wheel . . . . .	3
2.2 Pearlite morphology . . . . .	4
2.3 Crack initiation and crack propagation . . . . .	5
2.3.1 Crack propagation modes . . . . .	5
2.3.2 Rolling contact fatigue . . . . .	5
2.4 Anisotropy . . . . .	7
2.4.1 Methods for producing anisotropic pearlitic steel . . . . .	7
2.4.2 Evolution of microstructure alignment . . . . .	7
2.4.3 Mechanical properties of anisotropic pearlitic steel . . . . .	8
2.5 Strength of pearlite . . . . .	8
2.5.1 Yield strength . . . . .	8
2.5.2 Work hardening . . . . .	9
2.6 Pre-deformation - Replication . . . . .	9
2.7 Dislocation theory . . . . .	10
<b>3 Experimental</b>	<b>13</b>
3.1 Pre-deformation . . . . .	13
3.2 Hardness and shear strain - <b>Paper A</b> . . . . .	14
3.3 Uniaxial fatigue crack propagation - <b>Paper A</b> . . . . .	15
3.4 Torsional fatigue crack propagation - <b>Paper B</b> . . . . .	16
3.5 Stiffness measurement - <b>Paper B</b> . . . . .	17
<b>4 Results from appended papers</b>	<b>19</b>
4.1 Hardness and shear strain measurement . . . . .	19
4.2 Crack measurement and crack path - Paper A . . . . .	20

4.3	Fatigue life and crack path - Paper B . . . . .	24
<b>5</b>	<b>Conclusions</b>	<b>29</b>
<b>6</b>	<b>Future work</b>	<b>31</b>
	<b>References</b>	<b>33</b>
<b>II</b>	<b>Appended Papers A–B</b>	<b>37</b>



# Part I

## Extended Summary

### 1 Introduction

#### 1.1 Background

The impacts from global warming and climate change will continue to increase as the global greenhouse gas emissions reaches new peak levels every year. The consequences of this development must not be underestimated. In order to meet our needs in the near and long term, we must move towards a climate-neutral society. This is a great challenge which involves every sector of society, and not least the transportation sector. Transportation alone stood for 16.2 % of the CO<sub>2</sub> emissions in 2016 [1] and reducing the emissions to net-zero is therefore of great significance. The need of energy efficient and climate neutral means of transportation makes rail transportation a good candidate. Rail transportation is one of the most energy efficient and safest modes of transportation. It has the potential to play an important role in the net-zero transition. However, this is provided that safety, functionality and reliability as well as economic feasibility can be ensured. The major material related challenge is rolling contact fatigue which impairs safety and reliability as well as the economic feasibility. Understanding how the mechanical behavior and material properties in wheels and rails change in service and how this evolution effect crack initiation and crack propagation is one key factor to mitigate the effect of rolling contact fatigue.

The area of the contact patch between the railway rail and wheel have the size of a small coin and axial loads between 6-12 tonnes are typical static levels. Thus the contact stress becomes very high. In addition to axial load, the rail is also subjected to frictional forces resulting from traction, cornering and flange contact. The frictional forces can cause the surface material to become severely deformed. The microstructure of the severely deformed material is aligned and the mechanical behavior is anisotropic. It is well known that many defects associated with rolling contact fatigue is initiated at the severely deformed surface. However, the material properties and mechanical behavior of the severely deformed surface material is not fully understood.

Previous projects (M24, MU27, MU28, MU34) conducted within the research group Chalmers Railway Mechanics (CHARMEC) have investigated the severely deformed surface material. A predeformation method for replicating the material state close to the surface of deformed rail was developed. The microstructure, yield surface and local strength was characterized and the evolution of anisotropy with predeformation modelled. This project is a continuation of the previous work and is focused on the effect of anisotropy on fatigue crack initiation and propagation. The aim is to better understand how the anisotropy developing in service changes the fracture and fatigue characteristics of rail and wheel material.

## 1.2 Aim and scope

The predeformation method, which replicates the material state close to the surface of rails forms the foundation of the experimental work in this thesis. The main focus has been on the effect of large shear deformation on the fatigue crack behavior of pearlitic rail steel. The aim was to better understand the relation between crack propagation resistance, crack path and degree of anisotropy. The objectives are summarized as follows:

- Investigate the effect of predeformation on the crack growth direction and crack propagation rate under uniaxial fatigue loading. This was done in **Paper A**.
- Investigate the effect of predeformation on the crack growth direction and fatigue life under pulsating torsional loading, along and against the direction of predeformation, with and without a superimposed axial load. This was done in **Paper B**.

## 2 Theory

### 2.1 Railway-wheel

The geometry of a typical rail-wheel interface is shown in figure 2.1. On straight tracks and curves with large radii, the running band/surface of the wheel and rail are in contact. This contact condition generates the lowest contact stresses and lateral forces. In tighter curves, the contact condition becomes much more severe because then the wheel flange is in contact with the gauge corner of the rail. This is the contact condition responsible for the severely deformed surface material, commonly observed in the near-surface region of the gauge corner [2]. The load condition, as described, is dependent on the wheel-rail contact which varies along the rail. The wheel-rail contact also varies over time as wear and plastic deformation cause the geometry of the rail and wheel profiles to change. In addition, the load condition is dependent on the train type, accelerations and speeds. Thus, it can be concluded that the load history of the rail and wheel is complex and therefore very difficult to predict. As the associated material damage is dependent on the load history, it becomes challenging to evaluate and fully understand.

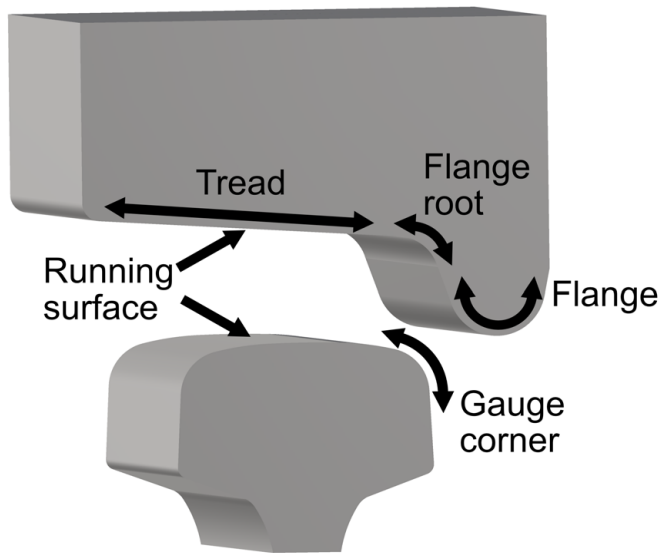


Figure 2.1: Geometry of a typical wheel-rail interface.

## 2.2 Pearlite morphology

Pearlitic steels have a two-phase microstructure composed of alternating lamellae of ferrite and cementite. The formation of pearlite occurs by an eutectoid reaction where austenite is transformed to ferrite and cementite by diffusion. The morphology of the pearlitic microstructure is shown in figure 2.2. The grains are called nodules and are formed on prior austenite grain boundaries by the growth of pearlite colonies. The nodules contain several differently oriented colonies [3]. The orientation of the ferrite and cementite lamellae within each colony is similar and the boundary between the lamellae is semi-coherent [4].

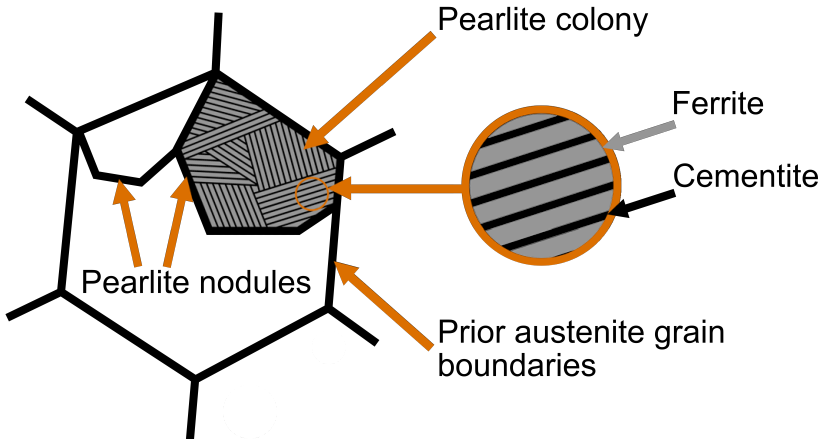


Figure 2.2: Morphology of the pearlitic microstructure.

The formation of pearlite from austenite can be obtained by either continuous cooling or isothermal cooling. The interlamellar spacing can be tailored with both methods because it is controlled by the diffusion rate of carbon [5]. In isothermal cooling the interlamellar spacing is controlled by the degree of undercooling where a decrease in holding temperature decreases the interlamellar spacing. Similarly, increasing the cooling rate during continuous cooling decreases the interlamellar spacing [6]. The interval within which pearlite is formed is described by the time temperature transformation (TTT) diagram and continuous cooling transformation diagrams (CCT) respectively.

## 2.3 Crack initiation and crack propagation

### 2.3.1 Crack propagation modes

Cracks can propagate under different loading modes and the loading mode/s under which a crack propagates can be divided into three basic modes as visualized in 2.3. Mode I is the opening mode in which the crack is loaded in tension perpendicular to the crack plane. Most cracks in engineering propagate under mode I loading. Crack propagation under a shear load is called mode II or mode III depending on the relative orientation of the shear load with respect to the crack plane. Mode II is the shear mode and results when the applied shear load is parallel to the crack plane. In this case the crack faces slide over each other and the crack front is perpendicular to the applied shear load. Mode III is called tearing mode and in this case the crack front is instead parallel to the applied shear load [7], [8].

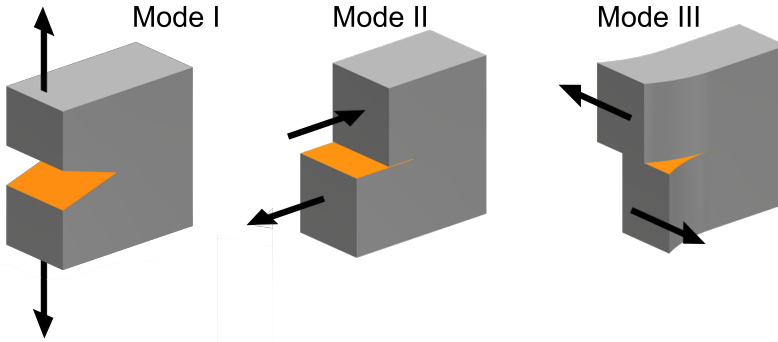


Figure 2.3: Three modes of crack propagation.

### 2.3.2 Rolling contact fatigue

Rolling contact fatigue is the process of crack initiation and crack growth in materials subjected to repeated rolling contact. Applications such as gears, rolling bearings, railway rails and wheels are subjected to rolling contact fatigue. Fatigue crack propagation due to rolling contact fatigue is different from classical fatigue since cracks predominantly grow under a compressive load. The contact stresses developed at the rail-wheel contact arise from the wheel load and frictional forces due to traction, cornering and braking. The imposed loading condition induce a multiaxial and non-proportional compressive stress state [9]. This stress state is dependent on numerous factors including the size and location of the contact patch, magnitude of the imposed loads, surface condition and rail grade [10]. Crack initiation is generally preceded by plastic deformation and the load history of the material will govern the propensity for crack initiation, the number of initiated cracks, the location of crack initiation as well as crack initiation angle [11, 12, 13].

Examples of different rolling contact fatigue cracks are illustrated in figure 2.4. Cracks can either be surface or subsurface initiated. Figure 2.4a shows the case of a subsurface initiated crack due to a vertical load on a rolling object [14]. Subsurface initiated cracks of this kind is usually related to material defects such as magnesium sulfides. The rolling contact loading in figure 2.4a can also cause a surface initiated crack in the presence of a surface asperity as shown in figure 2.4c. The surface asperity is a stress raiser which promote crack initiation.

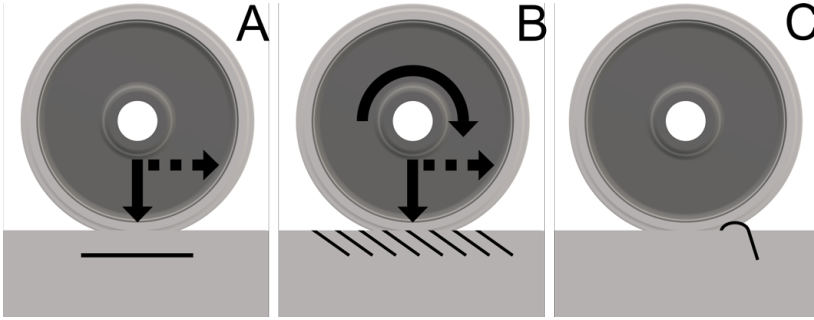


Figure 2.4: Examples of rolling contact fatigue cracks, modified from [14].

The most commonly observed rolling contact fatigue crack in rails is illustrated in figure 2.4b and figure 2.5, for more examples on rail defects see [15]. These cracks are called head checks and occur when material is subjected to both vertical and shear loads. The shear loads cause severe plastic deformation of the rail surface. Severe plastic deformation occurs when the magnitude of the interfacial shear stresses from traction, cornering and braking repeatedly exceeds the yield strength. This occur for unidirectional traffic when the wheel flange is in contact with the gauge corner of the rail [9]. The interfacial shear stresses leads to accumulation of shear strains which cause hardening and alignment of ferrite and cementite lamellae in pearlitic steels [16], [17]. Crack initiation occurs when the fracture strain is exceeded and subsequent crack growth occurs along direction of the microstructure alignment [18]. These cracks mainly grow under mixed mode II and III loading as mode I propagation is suppressed by the compressive stress in the contact zone. As the crack grows deeper, into undeformed material and out of the contact zone, crack growth is deviated into mode I growth. The crack can then either propagate downwards or upwards depending on the weakest path and bulk stresses. The rate of the mix-mode crack propagation is dependent on the crack face friction. Increasing friction reduces the rate of crack propagation. Thus, lubrication increase crack propagation. However, lubricating rails reduce the risk of crack initiation [9],[8].



Figure 2.5: Head checks on the gauge corner of the rail.

## 2.4 Anisotropy

### 2.4.1 Methods for producing anisotropic pearlitic steel

Anisotropy refers to directional dependent physical properties of a material e.g. directional dependent strength. Severely deformed pearlitic steels have a strong crystallographic texture and their mechanical properties are anisotropic. The crystallographic texture development at the severely deformed surface layer of rail steels requires large accumulation of shear strains. Several processing techniques are available to produce severely deformed pearlitic steel. The most common method is wire drawing but the applied loading condition is not similar to the rail-wheel contact, see e.g. [19] and [20]. High pressure torsion is another processing technique that can be used in which the material is deformed by large shear strain under the application of large compressive hydrostatic stresses, see e.g. [21] and [22]. Thus, the load condition is very similar to that of the rail-wheel contact and with this method a material state similar to the severely deformed surface of rail can be produced. The severe deformation of the material is made possible through the high hydrostatic pressure which suppresses crack initiation and propagation. From a railway perspective the evolution of microstructure and mechanical properties of pearlitic steels subjected to high pressure torsion is of special interest to study.

### 2.4.2 Evolution of microstructure alignment

The microstructure of pearlitic steels aligns along the direction of the applied load when subjected to medium and large strains. The deformation also cause thinning of the lamellae i.e., a decrease in interlamellar spacing. At very high strains the lamellae in wires becomes parallel to the drawing direction and in high pressure torsion parallel to the shear direction [19], [21]. The high straining also leads to dissolution of cementite [23]. At the microscopic scale the alignment is not perfect. The reorientation of the cementite lamellae is dependent on initial orientation with respect to the load axis. Unfavorable orientation cause the cementite lamellae to bend and fracture [19],[23],[24]. Wavy and fragmented lamellae are not uncommonly observed in the surface layer of rails subjected to severe deformation, see e.g. [25],[26],[27].

### 2.4.3 Mechanical properties of anisotropic pearlitic steel

Fracture toughness and fatigue crack propagation rate have been found to be a strong function of the ferrite-cementite orientation. The fracture toughness of pearlitic steels deformed with high pressure torsion is dependent on the relative orientation between the crack plane and cementite lamellae. Crack plane oriented parallel to cementite lamellae exhibit the lowest fracture toughness, lower than for undeformed pearlite. The fracture toughness on the other hand increase for crack planes perpendicular to the cementite lamellae [21],[22]. The observed anisotropy is attributed to the lamellae alignment. The fatigue crack propagation rate follows the same trend where an increase in crack propagation rate is observed for crack planes oriented parallel to the cementite lamellae. The trend was observed for equivalent von Mises strains of 2 and upwards [28], [29].

## 2.5 Strength of pearlite

### 2.5.1 Yield strength

The yield strength of undeformed pearlitic steels is primarily controlled by the interlamellar spacing. The strong influence of the interlamellar spacing have been explained on the basis of an effective slip distance [6], [30], [31]. Dislocations cannot continue their movement through the cementite lamellae and thus the interlamellar spacing controls the available slip distance. Thus, a decrease in interlamellar spacing increases the yield strength as it becomes more difficult to move the dislocations upon macro-yielding. The explanation is based on the assumption that dislocation sources becomes activated in a micro-yield region at the ferrite-cementite interface i.e. dislocations are generated at low strains prior macro-yielding. The assumption of activated dislocations sources at the ferrite-cementite interface have been proven to be valid by transmission electron microscopy. According to Dollar et al [31], microyielding could be explained by incompatibility strains between the ferrite and cementite lamellae. The yield strength of pearlitic steels can be approximated with equation (1) which is a Hall-Petch equation type equation with respect to the interlamellar spacing. The equation have been established through regression analysis.

$$\sigma_y = \sigma_0 + \frac{k_y}{\sqrt{S}} \quad (2.1)$$

Where  $\sigma_y$  is the resulting yield stress. The interlamellar spacing is denoted by  $S$  and the material constants  $k_y$  and  $\sigma_0$  corresponds to the lattice friction stress and dislocation locking (contribution of from work hardening) respectively.

Additional strengthening mechanisms contribute to the yield strength of deformed pearlite. Zhang [19] investigated the evolution of yield strength in cold drawn pearlitic wires by successive straining. Microstructural analysis identified three strengthening mechanisms that contribute to the observed yield strength with strain, namely: grain boundary strengthening, dislocation hardening and solid solution hardening. The yield strength could successfully be estimated by linear addition of the individual contributions for the investigated range of drawing strain. The solid solutions strengthening mechanism is based on cementite dissolution causing carbon enrichment of ferrite. Cementite dissolution



have been observed in severely deformed pearlitic steels. The grain boundary strengthening is based on the interlamellar spacing which decrease with drawing strain and act as barrier for dislocation movement. Dislocation strengthening is based on dislocation entanglement which increase with dislocation density. A similar study was conducted by Nikas et al [32] for pearlitic rail steel deformed by torsion under compression. The increase of yield strength with shear strain was attributed to dislocation hardening and grain boundary hardening.

### 2.5.2 Work hardening

Plastic deformation of pearlitic steels is inhomogeneous owing to differences in mechanical properties of the two phases (ferrite and cementite) and differences in the orientation of nodules and lamellae throughout the structure. Internal stresses denoted according to its origin namely phase stress, block (nodule) stress and colony stress are thus generated upon plastic deformation [33]. In-situ neutron diffraction of pearlitic steels during tensile deformation have confirmed this strain inhomogeneity [33, 34, 35, 36, 37, 38]. The elastic strain of the constituent phases of undeformed pearlite remained equal up to the onset of macro-yielding as the elastic moduli are similar. The yield stress of cementite is considerably higher than that of ferrite which cause stress partitioning at the onset of yielding. It was found that this stress partitioning is the governing mechanisms for the high work-hardening observed in undeformed pearlitic steels. The cementite is mainly elastically deformed whilst the ferrite phase is plastically deformed. The average stress in the structure could be approximated with a rule of mixtures based on the volume fraction of cementite and the measured elastic strain in each respective phase [38]. The degree of work hardening was found to be independent of interlamellar spacing and prior dislocation density. In conclusion, the yield stress is governed by the hardness of ferrite which depend on solid solution strengthening, dislocation hardening and interlamellar spacing but the increase in dislocation density during plastic deformation does not significantly affect the degree of work hardening [35].

## 2.6 Pre-deformation - Replication

Understanding the material properties and mechanical behavior of the severely deformed surface layer requires extensive mechanical testing and material characterization. However, in practice the material state is very difficult to evaluate. The difficulties originate from the high and non-linear strain gradient present in the severely deformed surface layer. Moreover the surface layer is very thin and the degree of plastic deformation varies along the rail. Thus, if test bars of reasonable size were to be extracted the material state would be heterogeneous and difficult to replicate.

The material state can be replicated through the application of hydrostatic compressive stress and shear stress. Equal angular channel pressing, and high-pressure torsion are two severe plastic deformation techniques that have been used previously in research to replicate the severely deformed surface layer [21, 22, 28, 29, 39]. These methods can achieve a shear strain magnitudes similar to that of field samples. However, the size of the

samples that can be extracted is very limited making it difficult to achieve axi-symmetrical specimens which are required for multiaxial fatigue testing.

Meyer [40, 16] developed a method capable of replicating the material state in axi-symmetric test bars by twisting cylindrical test bars under a constant compressive load. This method can achieve shear strains up to 2.3 in standard test bars with 10 mm diameter gauge. The material state was shown to be representative for the material state in the severely deformed layer with equal amount of shear strain. The microstructure obtained with this method is shown in figure 2.6. The main drawback with this method is that shear strains at a level as high as found the very top surface of the rails cannot be achieved.

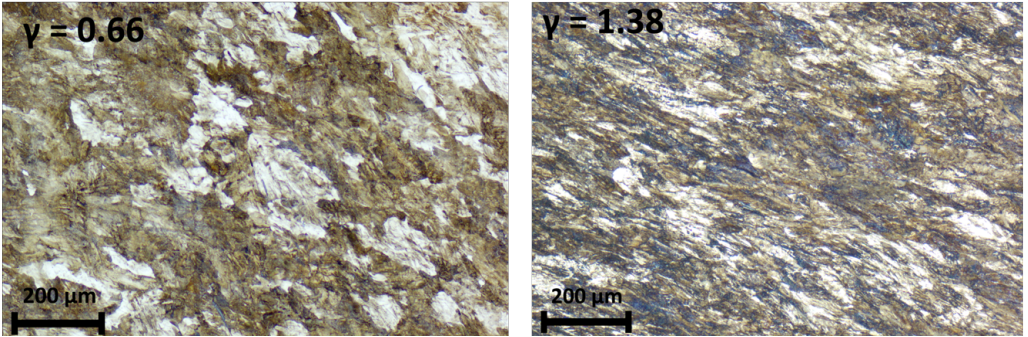


Figure 2.6: Microstructure obtained by predeforming axi-symmetric test bars through torsion under a constant compressive load.

## 2.7 Dislocation theory

Plastic deformation is defined as permanent deformation. In metals, plastic deformation occurs by slip and/or twinning. The deformation mechanism in pearlitic steels is restricted to slip which can be defined as the relative movement between two atomic planes by the motion of dislocations. Dislocations are line defects and exists in all polycrystalline materials. There are two basics types, edge dislocations and screw dislocations. In general, dislocations are mixed, having the character of both edge and screw. Movement of dislocations requires an imposed shear stress of a certain magnitude which is dependent on the microstructure and crystal structure as well as the dislocation density and composition [41].

The ideal slip process with an edge dislocation, starting off from an initial perfect 3-dimensional lattice is illustrated (in two dimensions) in figure 5. The applied shear stress breaks the lattice and introduce the dislocation in figure 5b. The edge dislocation is an extra atomic half plane. Dislocation movement through the lattice (figure 5c-f) occurs under the application of an applied shear stress by breaking the bonds connecting the lower half plane to the neighboring lattice plane. Thus, the dislocation is moved by shifting its position i.e. the atoms of the dislocation in figure 5b and figure 5c are not the same. The slip step is produced in figure 5e as the dislocation reached a free surface [41].

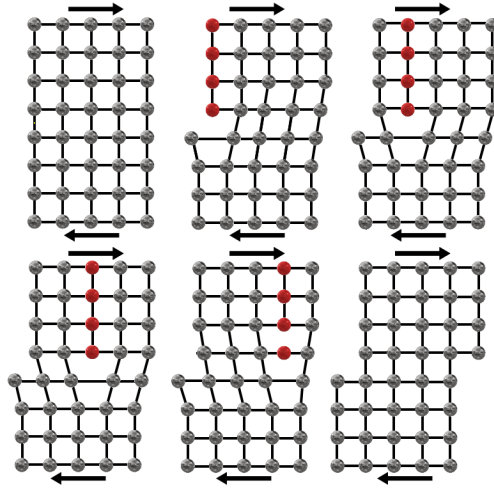


Figure 2.7: Illustration of deformation by slip with an edge dislocation.

Dislocations can only glide along specific crystallographic planes called slip planes and in specific directions called slip directions. In general slip planes are the most dense planes and the slip direction is the most closed packed direction. The active slip plane is in general the plane with the highest resolved shear stress. However, slip in body center cubic (bcc) metals such as pearlitic steels is anomalous. In bcc metals, there exist only one close packed direction but no closed packed planes. The slip direction is  $\langle 111 \rangle$  and the most dense planes are  $\{110\}$ ,  $\{112\}$  and  $\{123\}$  which all have the same density. The most common slip plane in iron is  $\{110\}$  and three of these planes intersect along the  $\langle 111 \rangle$  direction. The intersection makes it possible for cross-slip and therefore slip is often not well defined and wavy. Moreover, the active slip plane/s within the slip system is dependent on composition, crystal orientation, temperature and strain rate [41].



## 3 Experimental

### 3.1 Pre-deformation

The predeformation method developed by Meyer in [40] have been used in this thesis work to replicate the material state of the severely deformed surface layer. The material state is obtained by repeatedly twisting solid cylindrical test bars while applying a constant compressive force, as described and illustrated in figure 3.1. Test bars subjected to the predeformation process undergo geometry changes, manifested as a diameter increase and shortening of the gauge section. Reprofilng is required after predeformation because test bars for fatigue testing needs to be axi-symmetric.

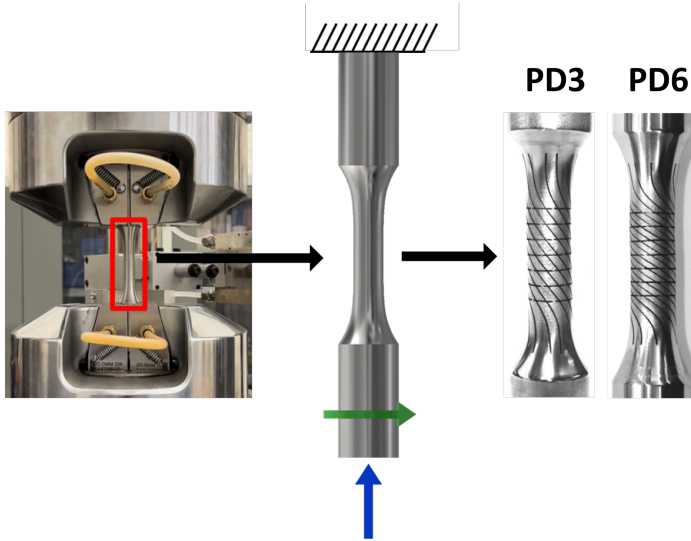


Figure 3.1: Illustration and description of the predeformation method. Test bars with deformed grid corresponding to PD3 and PD6 is included.

In **Paper A**, test bars with an gauge section diameter of 10 mm were predeformed under an constant force of 39.27 kN which corresponds to an initial nominal stress of -500 MPa. The material was predeformed to two different material states, denoted as PD3 and PD6 which corresponds to twisting  $3 \times 90^\circ$  and  $6 \times 90^\circ$  respectively. Prior predeformation a laser etched grid was imprinted. The deformed grid for PD3 and PD6 test bars is shown in figure 3.1. The angle between the grid lines was measured to calculate the surface shear strain. In **Paper B**, test bars were predeformed to PD3 with the same predeformation parameters and test bars geometry as in **Paper A**.

### 3.2 Hardness and shear strain - Paper A

The hardness was measured on both undeformed and predeformed material with the hardness tester DuraScan 70 G5 from Struers/Emcotest. Hardness indents were made on the axial cross-section of the gauge section according to the pattern in figure 3.2. Hardness was measured after reprofiling and after uniaxial fatigue crack propagation. To avoid influence of plastic deformation caused by the notch and the growing crack the samples were cut out 2.6 mm from the center of the gauge section. In addition, a reference sample was extracted to verify that hardness of the samples were unaffected by the fatigue crack propagation experiments. The applied load was 5 kgf (HV5) for all samples.

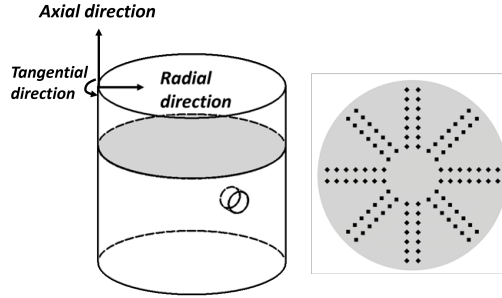


Figure 3.2: Illustration of the hardness pattern used for characterizing the hardness gradient.

The shear deformation of the predeformed test bars was evaluated by measuring the surface shear strain. The surface shear strain was calculated as  $\gamma = \tan(\alpha - 90^\circ)$  by measuring the angle between the intersecting lines, as illustrated in figure 3.3. In total, the angle was measured at 24 positions. To avoid influence of the test bar curvature, the angle was measured along the center line of the test bar. In total, 20 test bars were measured, 10 of each predeformation state (PD3 and PD6).

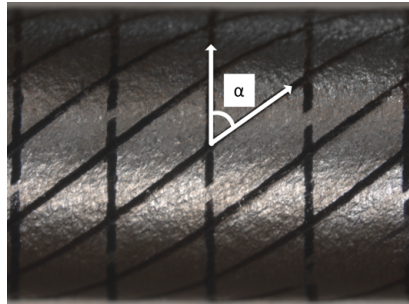


Figure 3.3: Shear strain measurement of predeformed test bars.

### 3.3 Uniaxial fatigue crack propagation - Paper A

The uniaxial fatigue crack propagation experiments were conducted on undeformed (PD0) and predeformed (PD3 and PD6) pearlitic steel (R260). The experiments were load controlled and conducted at a frequency of 10 Hz using a sinusoidal load waveform. In total, two nominal stress amplitudes with zero mean stress were used, corresponding to 60 % and 70 % of the offset yield strength in tension for undeformed material ( $Rp_{0.2} = 534.2$  MPa [40]). Test bars were mirror polished and notched prior fatigue testing. A starting notch in the shape of a drilled hole was used to create a stress concentration to steer crack initiation, see figure 3.4. The fatigue experiments continued until fracture.

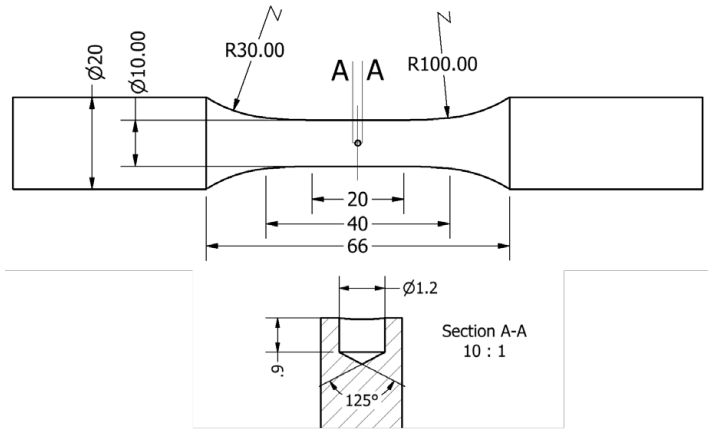


Figure 3.4: Dimensions and geometry of the notched test bars used in **Paper A**. Dimensions in mm.

Micrographs of the surface crack was acquired using both stereo -and optical microscope. Each micrograph represents the projection on the image plane as seen in figure 3.5. The crack width was measured on stitched images and corrected for the curvature of the test bar.

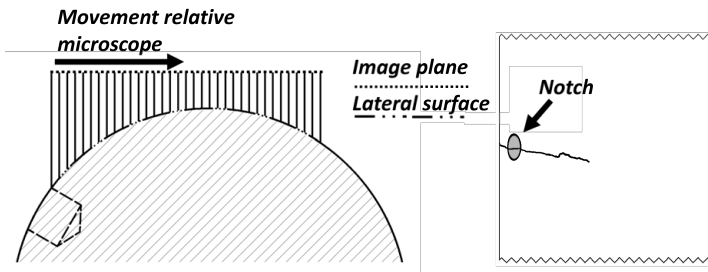


Figure 3.5: Illustration of crack measurement with stereo and optical microscope.

### 3.4 Torsional fatigue crack propagation - Paper B

Fatigue crack propagation experiments under pulsating cyclic loading were conducted on both undeformed and predeformed material (PD3). The fatigue experiments were strain controlled where torsional strain was controlled by the rotation angle  $\theta = 0.0132 \pm 0.0044$ , measured with a biaxial extensometer over its gauge length  $L = 12$  mm, as illustrated in figure 3.6. The strain interval was experimentally determined to achieve an initial torque response of 0 to 50 Nm for undeformed material. The waveform of the torsional load was sinusoidal and the test frequency was set to 1 Hz. The direction of the torsional load was either applied along or against the direction of predeformation, with or without a superimposed compressive axial load of -100 MPa, see table 3.1. Axial and torsional stiffness was measured every 1000th cycle and was used as a measure of the damage evolution during testing. The fatigue life was defined as the number of cycles until a 5 % drop from the initial axial stiffness. The test bars used in this study had a circumferential notch with a notch radii of 0.4 mm, see figure 3.6.

Table 3.1: Test matrix.

Predeformation	Direction	Axial load	Nr of test bars
PD0	Along	-100 MPa	3
PD0	Along	0 MPa	3
PD3	Along	-100 MPa	2
PD3	Along	0 MPa	2
PD3	Against	-100 MPa	1

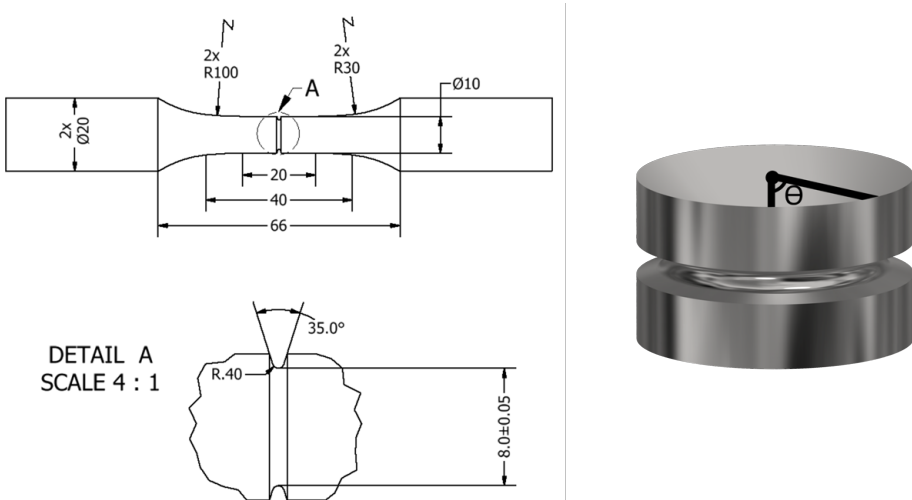


Figure 3.6: Geometry and dimensions of notched test bars and illustration of the measured rotation angle  $\theta$ . Dimensions in mm.



### 3.5 Stiffness measurement - Paper B

The stiffness measurement procedure is described in figure 3.7. The figure shows three measurement intervals in which the measured quantities are time averaged to reduce influence of measurement noise. The measured quantities were torque (T), rotation angle ( $\theta$ ), axial force (F) and axial strain ( $\epsilon$ ). Torque and rotation angle was used to calculate torsional stiffness according to equation (3.1). Similarly, axial force and axial strain was used to calculate axial stiffness according to equation (3.2). Torsional stiffness was measured under an axial load of 50 MPa to reduce the influence of crack face contact and axial stiffness was measured in unloading between 50 MPa and 20 MPa to reduce influence of plasticity and closing cracks.

$$\text{Torsional stiffness} = \text{abs} \left( \frac{T_1 - T_2}{\theta_1 - \theta_2} \right) \quad (3.1)$$

$$\text{Axial stiffness} = \text{abs} \left( \frac{F_1 - F_2}{\epsilon_1 - \epsilon_2} \right) \quad (3.2)$$

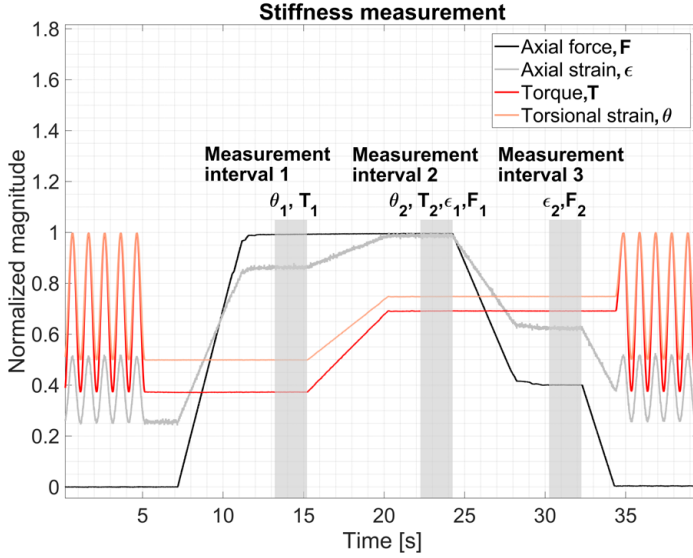


Figure 3.7: Measurement of axial and torsional stiffness.



## 4 Results from appended papers

### 4.1 Hardness and shear strain measurement

The hardness distribution of undeformed and predeformed material along the radial direction is shown in figure 4.1. In total, 112 indents were made for each test bar, evenly distributed over the different radial positions. The hardness distribution of undeformed material is uniform with an average hardness value of 269 HV5 and standard deviation of 7 HV5, which is in accordance with the material specification of the R260 steel, see EN 13674-4 [42]. Predeformation introduces an almost linear hardness gradient for both deformed material states. The hardness values are approximately 20 HV5 units higher in PD6 when compared to PD3. There is a good agreement of hardness values between similar shear strains, as seen by the parallel hardness curves of PD3 and PD6. The reference sample overlaps with the hardness curves of PD6, showing that plastic deformation was initially confined in a region close to the notch and later to the crack front.

The hardness distribution from a solid mechanics perspective can be explained by the stress and strain distribution. During torsion, every cross-sectional plane can be assumed to remain planar and thus the shear strain will linearly decrease towards the center. The stress distribution is however unknown as plastic deformation and thickening of the gauge section occurs during predeformation. It is the induced stress and strain gradient that causes radial differences in hardening. At the microstructural level, the hardness gradient is primarily explained by differences in dislocation density which increase with shear strain as reported by Nikas et al. [32].

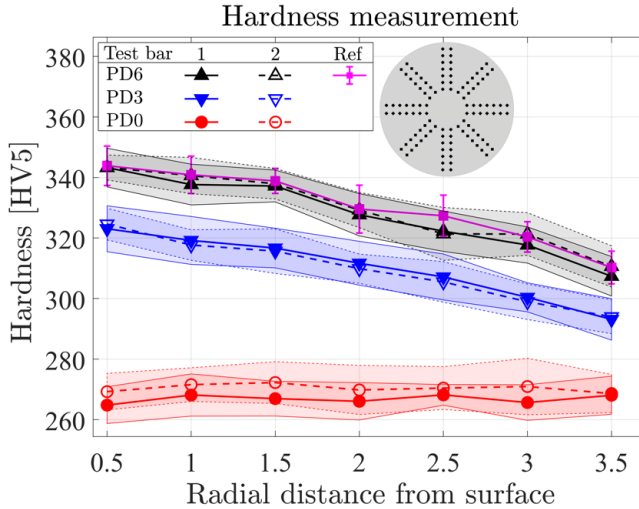


Figure 4.1: Hardness measurement of undeformed and predeformed test bars.

The shear strain measurements are given in table 4.1. Two columns are shown, the shear strain after predeformation and the shear strain after reprofiling. The standard deviation is low and with respect to the hardness measurements the predeformation method can be considered to have good repeatability.

Table 4.1: Shear strain measurement

	PD3	PD6
Average surface shear strain after pre-deformation	$0.74 \pm 0.05$	$1.52 \pm 0.05$
Average surface shear strain after reprofiling	$0.66 \pm 0.05$	$1.38 \pm 0.05$

## 4.2 Crack measurement and crack path - Paper A

The crack width measurement for the nominal stress amplitudes corresponding to 60 % and 70% of the offset yield strength of virgin rail material are shown in figure 4.2 and 4.3. For each test bars there are two measured cracks, one for each side of the notch. The crack propagation rate is initially constant and as the crack propagates a transition to exponential crack growth occur, except for the undeformed material at the larger load amplitude. Transition to exponential crack growth is expected as the load on the crack is a function of the area reduction (exponential increase). The area reduction is initially negligible and the stress intensity around the notch dominate the local stress condition. In each experiment, the crack propagation rate of the two cracks in each test bar is similar. This indicate that the two cracks initiated on each side of the notch joins to form a semi-elliptical crack after some growth.

Comparing the crack propagation resistance of undeformed and predeformed material a significant difference can be observed. The fatigue crack propagation resistance was for both load amplitudes highest in predeformed material. At the lower load amplitude the predeformed material endured almost twice the number of cycles of undeformed material for the same crack width. The difference between undeformed and predeformed material is even larger for the higher load magnitude. In this case, the interval between the crack length measurements are too long to judge the progression of the crack width. The crack propagation resistance of the predeformed material states PD3 and PD6 is very similar for the lower load amplitude. Expect one discrepancy where test bar 1 of PD3 had about 25 % longer fatigue life. The difference between PD3 and PD6 is larger for the higher load amplitude but still not drastic.

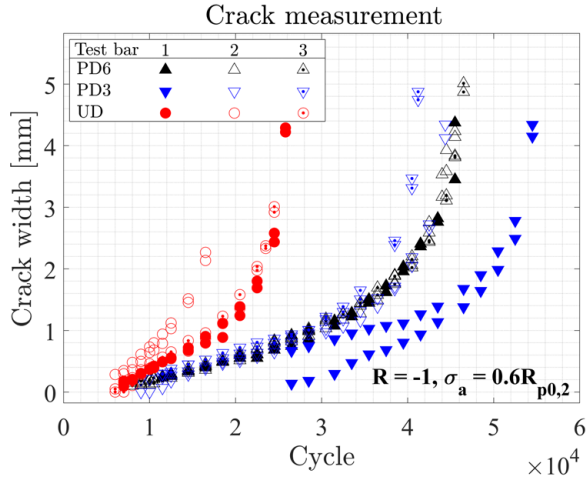


Figure 4.2: Crack propagation measurement from test bars subjected to a load amplitude of 60 % of the offset yield strength.

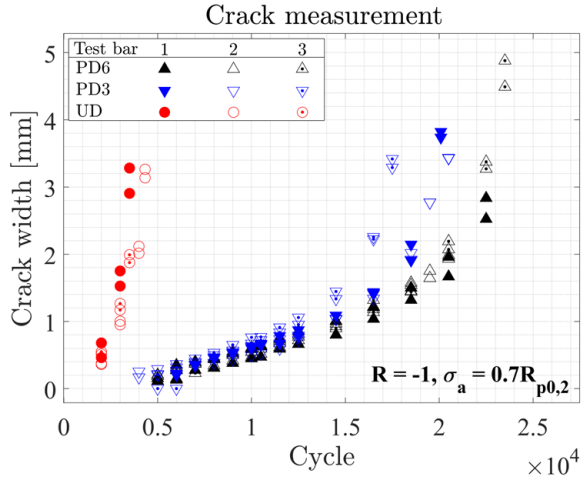


Figure 4.3: Crack propagation measurement from test bars subjected to a load amplitude of 70 % of the offset yield strength.

The correlation between crack path and material state was visualized by digitizing the crack surface contours of the final cracks. The crack contours were extracted in a commercial photo editing software and later processed with a Matlab script which converts the pixel data into spatial data. The digitized cracks are shown in figure 4.4 and 4.5 for respective load amplitude. The overlayed grid represent the surface shear deformation of PD6 in the direction towards which the microstructure is deformed. The crack growth direction for undeformed material and PD3 at both load amplitudes is on average straight with local crack kinking. The crack paths of PD6 shows a similar trend but with a slight inclination angle at the lower load amplitude. The results indicate that the crack path is influenced by the direction of the deformed microstructure if the magnitude of shear deformation is sufficiently high and the crack tip plasticity sufficiently low.

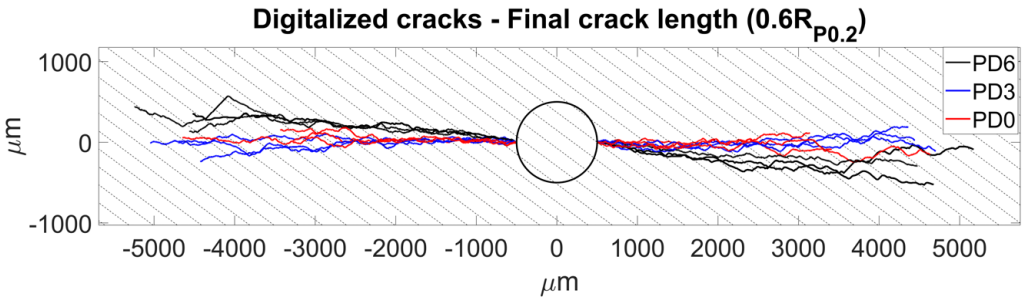


Figure 4.4: Digitized cracks for all test bars subjected to a nominal stress amplitude of 60% of the offset yield strength  $R_{p0.2}$ .

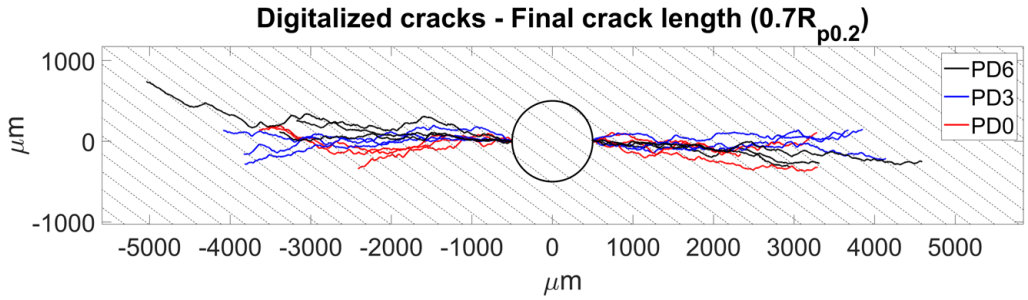


Figure 4.5: Digitized cracks for all test bars subjected to a nominal stress amplitude of 70% of the offset yield strength  $R_{p0.2}$ .

The crack growth direction was also examined with respect to the orientation of the cementite lamellae. The investigation showed a limited correlation between orientation of the cementite lamellae and the direction of crack growth. The variation in the relationship between crack growth and orientation of cementite lamellae for PD3 and PD6 is exemplified in figure 4.6a and 4.6b. In the figure it can be observed that there is a variation in crack growth direction and that the crack section-wise grows along the cementite lamellae. However, the surface crack path is not representative for the overall crack growth direction as the stress state close to the surface is mainly in plane stress and because the microstructure alignment varies along the radial direction.

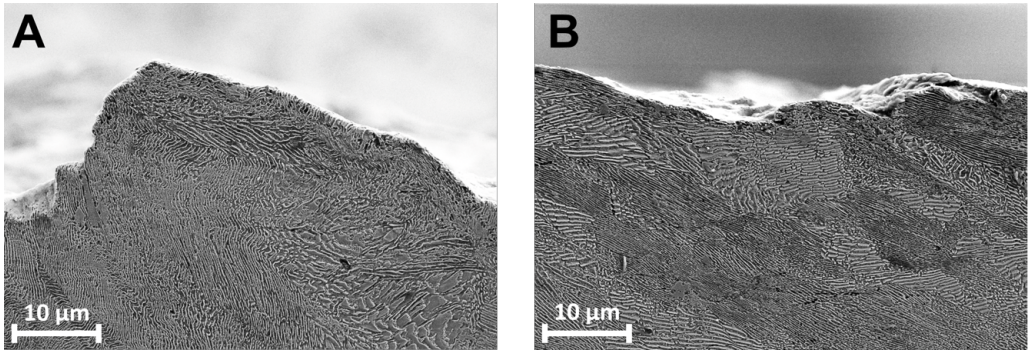


Figure 4.6: (a) and (b) show representative sections of surface crack growth for material states PD3 respectively PD6.

### 4.3 Fatigue life and crack path - Paper B

The stiffness measurements were filtered with a modified running average to reduce the scatter in the axial stiffness measurements. The filtered axial and torsional stiffness measurements are presented in figure 4.7 and 4.8, respectively. The axial stiffness measurements have a large scatter as shown by the standard deviation. This scatter stems from the low axial load applied during the axial stiffness measurement. However, the scatter in the torsional stiffness measurements are much lower as the torsional strain amplitude is higher than the axial strain amplitude. The variation between each repeated test is observed to be lower than the difference between the different test series. Thus, the axial stiffness measurements can be considered as sufficiently reliable.

The fatigue life, which was defined as a 5% drop in axial stiffness was observed to be dependent on the material state, axial compressive load and direction of the torsional load. The fatigue life is for both material states increased when an compressive axial load was applied. Predeformation slightly increase the fatigue life for torsional loading along the direction of predeformation. Reversing the torsional load significantly increases the fatigue life of predeformed material. This result was unexpected as cracks then grow along the predeformed microstructure.

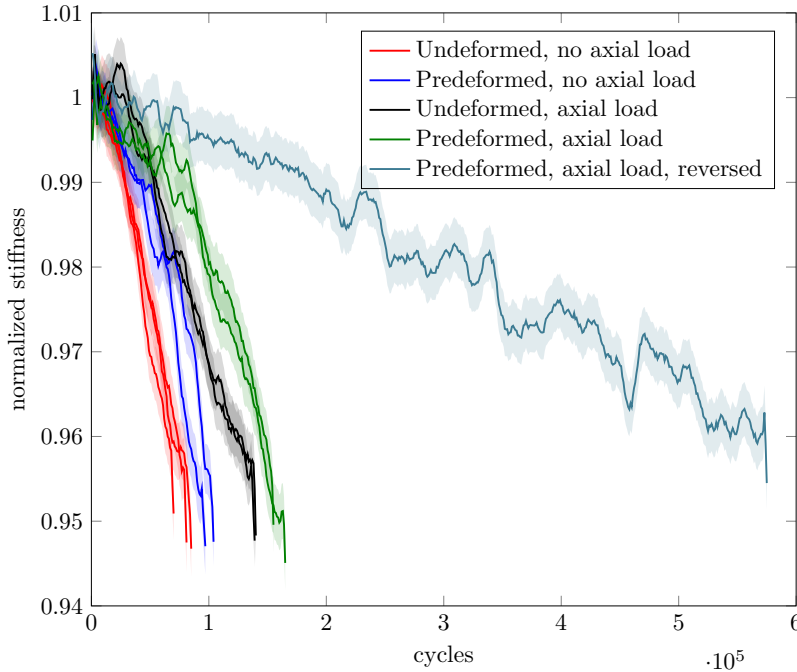


Figure 4.7: Axial stiffness evolution for different material and loading conditions. The colored areas show  $\pm$  one standard deviation.



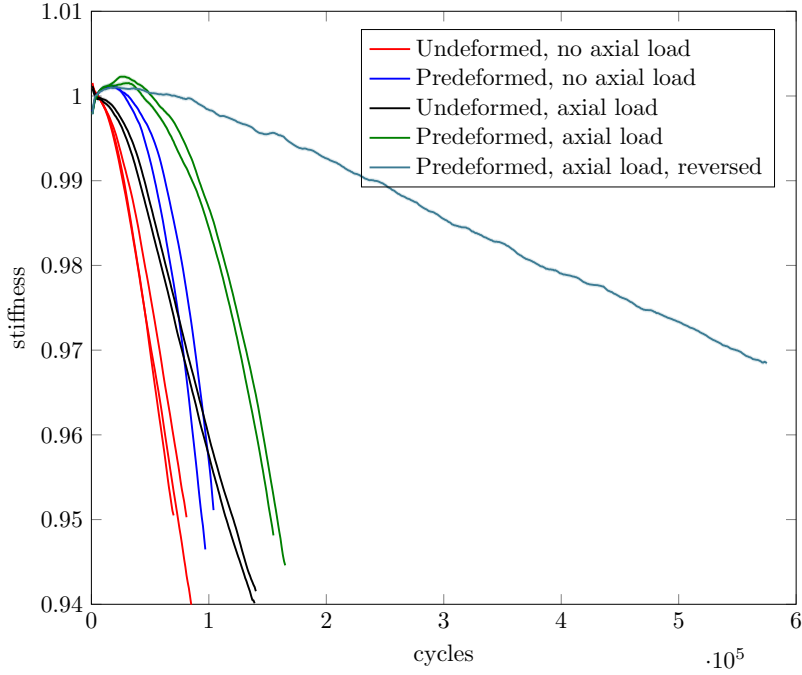


Figure 4.8: Torsional stiffness evolution for different material and loading conditions.

The fracture surfaces of all test bars were investigated. The crack growth direction and shape of the fracture surface was found to be dependent on the material state and load condition. In all experiments, fatigue crack growth is characterized by the growth of multiple cracks initiated along the circumference of the notch, resulting in a complex crack pattern. Crack growth was predominantly inclined in the clockwise direction for torsional loads along the direction of predeformation and along the counter clockwise direction when the torsional load was reversed. The fraction of cracks growing in the predominant direction was estimated by calculating the number and direction of cracks extending outside the notch, see table 4.2. The direction of inclined crack growth was found to correlate well with the direction of remote principal stress as discussed in **Paper B**. In addition, the predominant direction was found to be dependent on torque ratio  $R_{Torque} = \frac{T_{min}}{T_{max}}$ , where the the fraction of cracks growing in a predominant direction increase as the torsional load becomes more pulsating.

Material state	Axial load	Torsional load direction	Fraction of cracks
PD0	0 MPa	Along	67% CW
PD0	-100 MPa	Along	68% CW
PD3	0 MPa	Along	86% CW
PD3	-100 MPa	Along	87% CW
PD3	-100 MPa	Against	63% CCW

Table 4.2: Fraction of cracks counted in the predominant direction on the fracture surface. CW - Clockwise and CCW - Counter clockwise direction.

The fracture surfaces of undeformed material shows a similar appearance for all load conditions, see figure 4.9. The fatigue cracked zone (region of crack growth) is mainly continuous and extends rather uniform along the radial direction. However, there are regions along the circumference with no apparent fatigue cracks, as shown in insert 2 of figure 4.9. Characteristic for the fracture surfaces of undeformed material is the factory roof shaped fracture surface caused by primarily mode I crack growth. The factory roof of the fracture surface is asymmetrical with the longer side along the clockwise direction. The fracture surface of predeformed material subjected to torsional loading exhibited a similar fracture surface as undeformed material. The main differences observed was that the predominant crack growth direction is reversed and that the fatigue cracked zone in the radial direction was not as uniform.

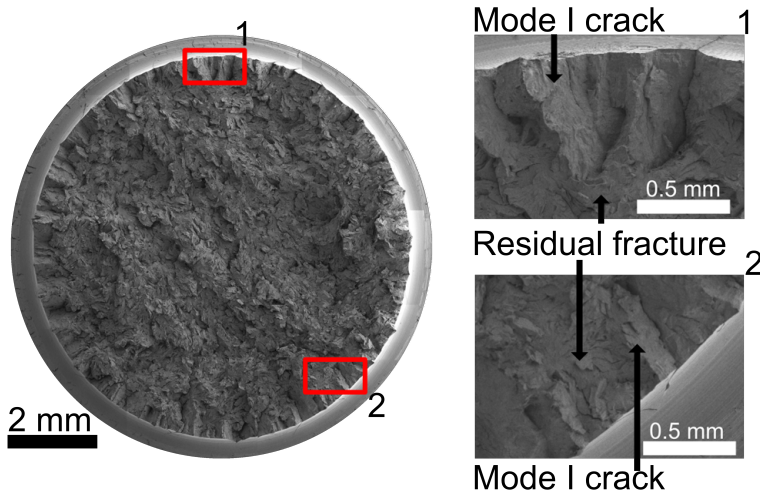


Figure 4.9: Representative fracture surface of undeformed test bars with shear load along the direction of predeformation.

The fracture surfaces of predeformed material subjected to torsional load along the direction of predeformation was significantly different from the undeformed material. In figure 4.10 a representative fracture surface of predeformed material subjected to axial load is shown. Characteristic for the fracture surfaces, with and without axial loading is the heterogeneous fatigue cracked zone. The axial load was observed to change the crack growth behavior. With axial load, a tendency of deeper crack growth was observed and crack growth was confined to fewer regions around the notch.

The complex crack network, characteristic for all experiments, was examined in more detail by transverse sectioning at different depths on the predeformed test bar in figure 4.10. The transverse lines a-c in insert 2 of figure 4.10 corresponds to the micrographs a-c in figure 4.11. The micrographs shows that crack growth occurred underneath what was observed as residual fracture on the topography. It can also be seen the cracks growth was against the direction of predeformation.

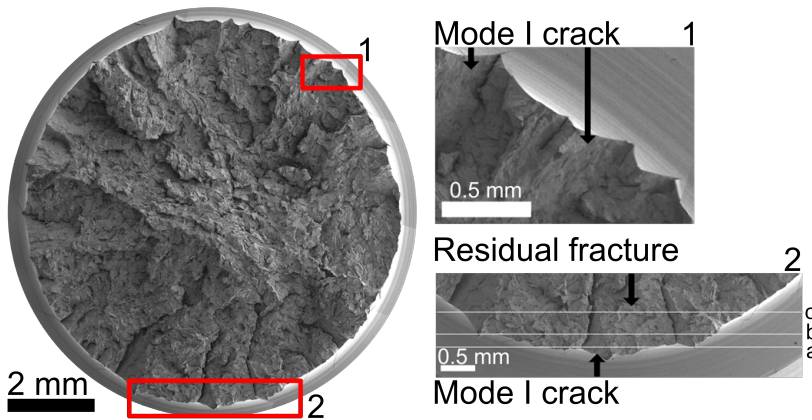


Figure 4.10: Representative fracture surface of predeformed test bars with axial load and shear load along direction of predeformation.

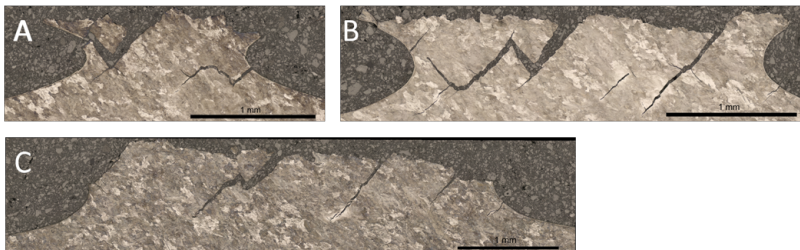


Figure 4.11: Radial view of crack network in a predeformed test bar at different depths from the notch root a) 51  $\mu\text{m}$  b) 234  $\mu\text{m}$  c) 547  $\mu\text{m}$ .



## 5 Conclusions

In **Paper A** the effect of larger shear deformation on crack propagation was investigated. The crack propagation rates in undeformed and predeformed material was measured and the crack paths were investigated. The investigation lead to the following conclusions:

- Fatigue crack propagation resistance is significantly higher in predeformed material under stress controlled, constant amplitude fatigue loading.
- Increasing predeformation from PD3 to PD6 has a limited effect on the fatigue crack propagation resistance.
- The crack growth direction does not follow the average direction of microstructure alignment.
- The crack path of both undeformed and pre-deformed material was tortuous.

In **Paper B**, a new fatigue test method under loading conditions similar to rolling contact loading, accounting for the large accumulated shear strains close to the surface, was proposed. The method has been applied to investigate the influence of accumulated shear strains, compressive stresses, and loading direction in the R260 rail steel. The main findings are:

- The torque range is similar for all cases, but the mean torque depends on predeformation and load direction.
- A compressive axial load has negligible influence on the mean torque but prolongs the fatigue life.
- The predeformed material sustains more cycles, even though the mean torque is increased for loading along the predeformation direction.
- Loading against the predeformation direction increases the fatigue life even though cracks grow in a weaker microstructural direction. This result was attributed to the lower mean torque.
- The crack growth direction is strongly correlated with the mean torque.
- Complex crack networks, similar to those observed in rail field samples, form around the notch.



## 6 Future work

The project will further consider fatigue crack propagation under multiaxial loading. Multiaxial fatigue crack propagation testing by combining axial and torsional load is more representative to the loading conditions at the rail/wheel interface and thus leads to a better understanding of how anisotropy affect crack propagation in the application. The fatigue crack propagation experiments will be conducted on test bars in both the undeformed and predeformed state. Digital image correlation will be implemented during fatigue testing to monitor crack initiation and potential drop will be considered for continuous crack measurement.





# References

- [1] H. Ritchie, M. Roser, and P. Rosado. CO and Greenhouse Gas Emissions. *Our World in Data* (May 2020).
- [2] R. Lewis and U. Olofsson. “Basic tribology of the wheel-rail contact”. *Wheel-Rail Interface Handbook*. Elsevier Ltd, Sept. 2009, pp. 34–57.
- [3] D. A. Porter, K. E. Easterling, and M. Y. Sherif. *Phase transformations in metals and alloys, third edition*. CRC Press, Jan. 2009, pp. 1–521.
- [4] N. Guo and Q. Liu. Back-scattered electron imaging combined with EBSD technique for characterization of pearlitic steels. *Journal of Microscopy* **246**.3 (June 2012), 221–228.
- [5] H. Bhadeshia and R. Honeycombe. “Iron-Carbon Equilibrium and Plain Carbon Steels”. *Steels: Microstructure and Properties*. Elsevier, Jan. 2017, pp. 59–100.
- [6] A. R. Marder and B. L. Bramfitt. The effect of morphology on the strength of pearlite. *Metallurgical Transactions A* **7**.2 (Feb. 1976), 365–372.
- [7] N. E. Dowling. *Mechanical Behavior of Materials - Engineering Methods for Deformation, Fracture, and Fatigue*. Pearson Education, 2012, pp. 1–960.
- [8] D. I. Fletcher, F. J. Franklin, and A. Kapoor. “Rail surface fatigue and wear”. *Wheel-Rail Interface Handbook*. Elsevier Ltd, Sept. 2009, pp. 280–310.
- [9] A. Ekberg and E. Kabo. “Fatigue of railway wheels and rails under rolling contact and thermal loading-an overview”. *Wear*. Vol. 258. 7-8. Elsevier, Mar. 2005, pp. 1288–1300.
- [10] S. Iwnicki, S. Björklund, and R. Enblom. “Wheel-rail contact mechanics”. *Wheel-Rail Interface Handbook*. Elsevier Ltd, Sept. 2009, pp. 58–92.
- [11] M. Schilke. *Thesis for the degree of doctor of philosophy - Degradation of Railway Rails from a Materials Point of View*. 2013.
- [12] A. F. Bower and K. L. Johnson. Plastic flow and shakedown of the rail surface in repeated wheel-rail contact. *Wear* **144**.1-2 (Apr. 1991), 1–18.
- [13] W. R. Tyfour, J. H. Beynon, and A. Kapoor. Deterioration of rolling contact fatigue life of pearlitic rail steel due to dry-wet rolling-sliding line contact. *Wear* **197**.1-2 (Sept. 1996), 255–265.
- [14] A. Ekberg, B. Åkesson, and E. Kabo. Wheel/rail rolling contact fatigue - Probe, predict, prevent. *Wear* **314**.1-2 (June 2014), 2–12.
- [15] *Rolling Contact Fatigue: A Comprehensive Review*. Tech. rep. 2011.
- [16] K. A. Meyer, D. Nikas, and J. Ahlström. Microstructure and mechanical properties of the running band in a pearlitic rail steel: Comparison between biaxially deformed steel and field samples. *Wear* **396-397** (2018), 12–21.
- [17] F. A. Alwahdi, A. Kapoor, and F. J. Franklin. Subsurface microstructural analysis and mechanical properties of pearlitic rail steels in service. *Wear* **302**.1-2 (Apr. 2013), 1453–1460.
- [18] M. Sato, P. M. Anderson, and D. A. Rigney. Rolling-sliding behavior of rail steels. *Wear* **162-164**.PART A (Apr. 1993), 159–172.
- [19] X. Zhang et al. Microstructure and strengthening mechanisms in cold-drawn pearlitic steel wire. *Acta Materialia* **59**.9 (May 2011), 3422–3430.

- [20] J. Toribio and E. Ovejero. Effect of cumulative cold drawing on the pearlite interlamellar spacing in eutectoid steel. *Scripta Materialia* **39.3** (July 1998), 323–328.
- [21] C. Kammerhofer et al. Influence of morphology and structural size on the fracture behavior of a nanostructured pearlitic steel. *Materials Science and Engineering A* **585** (Nov. 2013), 190–196.
- [22] A. Hohenwarter et al. “Effect of large shear deformations on the fracture behavior of a fully pearlitic steel”. *Metallurgical and Materials Transactions A: Physical Metallurgy and Materials Science*. Vol. 42. 6. Springer, June 2011, pp. 1609–1618.
- [23] Y. Ivanisenko et al. The mechanism of formation of nanostructure and dissolution of cementite in a pearlitic steel during high pressure torsion. *Acta Materialia* **51.18** (Oct. 2003), 5555–5570.
- [24] X. Zhang et al. Hierarchical structures in cold-drawn pearlitic steel wire. *Acta Materialia* **61.13** (Aug. 2013), 4898–4909.
- [25] J. E. Garnham and C. L. Davis. The role of deformed rail microstructure on rolling contact fatigue initiation. *Wear* **265.9-10** (Oct. 2008), 1363–1372.
- [26] L. Zhou et al. Comparison of the damage and microstructure evolution of eutectoid and hypereutectoid rail steels under a rolling-sliding contact. *Wear* **492-493** (Mar. 2022), 204233.
- [27] H. Chen et al. Microstructure evolution of a hypereutectoid pearlite steel under rolling-sliding contact loading. *Materials Science and Engineering A* **655** (Feb. 2016), 50–59.
- [28] T. Leitner et al. Influence of severe plastic deformation and specimen orientation on the fatigue crack propagation behavior of a pearlitic steel. *Materials Science and Engineering A* **710** (Jan. 2018), 260–270.
- [29] T. Leitner, A. Hohenwarter, and R. Pippan. Anisotropy in fracture and fatigue resistance of pearlitic steels and its effect on the crack path. *International Journal of Fatigue* **124** (July 2019), 528–536.
- [30] J. M. Hyzak and I. M. Bernstein. The role of microstructure on the strength and toughness of fully pearlitic steels. *Metallurgical Transactions A* **7.8** (1976), 1217–1224.
- [31] M. Dollar, I. M. Bernstein, and A. W. Thompson. Influence of deformation substructure on flow and fracture of fully pearlitic steel. *Acta Metallurgica* **36.2** (Feb. 1988), 311–320.
- [32] D. Nikas, X. Zhang, and J. Ahlström. Evaluation of local strength via microstructural quantification in a pearlitic rail steel deformed by simultaneous compression and torsion. *Materials Science and Engineering A* **737** (Nov. 2018), 341–347.
- [33] T. Shinozaki et al. Influence of Lamellar Spacing on Deformation Behavior of Pearlite Steels Studied by In Situ Neutron Diffraction (July 2022).
- [34] A. Kanie et al. Elastic Strains of Cementite in a Pearlite Steel during Tensile Deformation Measured by Neutron Diffraction. *ISIJ International* **44.11** (Nov. 2004), 1952–1956.
- [35] E. Gadalińska et al. Stress localisation in lamellar cementite and ferrite during elastoplastic deformation of pearlitic steel studied using diffraction and modelling. *International Journal of Plasticity* **127** (Apr. 2020), 102651.

- [36] H. Yahyaoui et al. Effect of interlamellar spacing on the elastoplastic behavior of C70 pearlitic steel: Experimental results and self-consistent modeling. *Materials and Design* **55** (Mar. 2014), 888–897.
- [37] Y. Wang et al. In-situ neutron diffraction during tension-compression cyclic deformation of a pearlite steel. *Materials Science and Engineering A* **676** (Oct. 2016), 522–530.
- [38] Y. Tomota et al. Effect of carbon concentration on tensile behaviour of pearlitic steels. *Materials Science and Technology* **19.12** (Dec. 2003), 1715–1720.
- [39] F. Wetscher, R. Stock, and R. Pippan. Changes in the mechanical properties of a pearlitic steel due to large shear deformation. *Materials Science and Engineering A* **445-446** (Feb. 2007), 237–243.
- [40] K. A. Meyer, M. Ekh, and J. Ahlström. Modeling of kinematic hardening at large biaxial deformations in pearlitic rail steel. *International Journal of Solids and Structures* **130-131** (2018), 122–132.
- [41] D. Hull and D. J. Bacon. *Introduction to Dislocations*. Elsevier Ltd, 2011.
- [42] EN13674-4. *Railway applications – Track – Rail – Part 4: Vignole railway rails from 27 kg/m to, but excluding 46 kg / m. EUROPEAN COMMITTEE FOR STANDARDIZATION*. Brussels, 2011.